J. Fluid Mech. (1989), *vol.* 205, *pp.* 319–340
Printed in Great Britain

Theoretical and numerical study of a three-dimensional turbulent boundary layer

By PHILIPPE R. SPALART
NASA Ames Research Center, Moffett Field, CA 94035, USA

(Received 10 August 1988)

The boundary layer is created on an infinite flat plate by a time-dependent free-stream velocity vector, whose magnitude is independent of time but whose direction (as seen in plan view) changes at a constant angular velocity. The pressure gradient, at right angles to the free-stream velocity, induces a skewing of the velocity profile; all components of the Reynolds-stress tensor are non-zero (using axes aligned with the wall and the flow direction). This flow has never been produced experimentally, but it has the merit of being simply defined and of having only the Reynolds number as a parameter, which greatly simplifies the analysis. The flow is studied theoretically using Reynolds-number scaling laws, and by direct numerical simulation over a range of Reynolds numbers. The simplest version of the theory is equivalent to existing theories of the Ekman layer. A higher-order version is presented and yields excellent agreement with the numerical results at three Reynolds numbers, with just one adjustable constant in each equation. The theory allows the extrapolation of the results to high Reynolds numbers. The Reynolds-averaged equations reduce to a one-dimensional steady problem, so that turbulence-model testing will be easy and accurate. Detailed data are provided for that purpose.

1. Introduction

We consider one of the simplest situations that can produce a boundary layer with three-dimensional statistics. A set of boundary conditions is described below that could be accommodated with our existing numerical method and allowed a fairly simple presentation of the results, but produced a flow with a skewed velocity profile and a full Reynolds-stress tensor. The direct simulations conducted until now included, of course, three dimensional fluctuations. However, their boundary conditions and therefore their turbulence statistics had a mirror-image symmetry in the z direction (for instance, the mean spanwise velocity and some elements of the Reynolds-stress tensor had to be zero by symmetry). There is now a drive to investigate in depth flows that are three-dimensional in the mean, because the flows of interest (planetary boundary layer, swept wings, curved ducts, and so on) are often strongly three-dimensional, and also because of the desire to extend and test some aspects of turbulence theory in more general situations (see the review by Bradshaw 1987).

The flow under study is similar but not identical to the prototype of atmospheric shear flows, the Ekman layer. The laminar solutions are identical, and the turbulent solutions are comparable. Many turbulence models (for instance mixing-length and two-equation models) would fail to distinguish between the present flow and the Ekman flow. Deardorff (1970) and Mason & Thomson (1987) presented large-eddy simulations of the Ekman layer. Direct simulations of that flow are now being

conducted and will be compared with the present ones (Coleman, Ferziger & Spalart 1989). The flow is also similar to the three-dimensional flows of interest in engineering, although we shall find that it is not strongly three-dimensional.

The present flow will probably not allow the validation of the numerical results by experiments (a very large facility would be needed), but we now have good confidence in direct simulations, and it has several decisive advantages. Like the two-dimensional oscillating flow studied by Spalart & Baldwin (1987, hereafter referred to as the SB flow) it is tractable numerically without any need for inflow/outflow conditions or approximations like the multiple-scale procedure applied to the spatially developing flat-plate boundary layer (Spalart 1988). The flow also loses memory of its initial condition. The turbulence statistics, when expressed in an appropriate reference frame and properly non-dimensionalized, depend only on the distance from the wall (and the Reynolds number). Thus the Reynolds-averaged equations are one-dimensional, which makes the present problem convenient and inexpensive for testing turbulence models. The analysis of the direct-simulation results and the collection of a statistical sample were also relatively easy; no phase-averaging or triple decomposition, such as the one used in the SB flow, was needed. The available computer resources allowed us to simulate the flow over a range of Reynolds numbers. Guidelines for the size of the domain and the grid spacing were obtained from previous work.

The theoretical work is an extension to higher order of that applied to the SB flow. These basic arguments were also applied by Kazanski & Monin (1961) (and more clearly by Csanady 1967) to the Ekman layer; they now appear in textbooks (Townsend 1976). One applies straightforward generalizations of well-known two-dimensional high-Reynolds-number scaling laws (e.g. the law of the wall) to three dimensions, and requires an overlap between an inner and an outer law. The analysis can be completed owing to the simplicity of the flows. It not only produces the usual equation linking the friction coefficient and the logarithm of the Reynolds number, but also an equation governing the angle α between the wall-shear-stress vector and the free-stream velocity. Each equation contains an unknown constant (in addition to the Kármán constant, which is not unique to this flow and is reliably known). These two global predictions, as well as some local predictions, are tested against the numerical results at three Reynolds numbers.

We adopted the approach of conducting direct simulations at rather low Reynolds numbers, and relying on a theory (with some empirical content) to extrapolate the results to higher Reynolds numbers (e.g. to obtain the friction coefficient). It is of course essential to first test the ability of the theory to interpolate between the results of simulations at different Reynolds numbers. In contrast, in a large-eddy simulation one uses a theory (also with some empirical content) to design a subgrid-scale model which is included in the simulations. The simulation can then be conducted at the desired Reynolds number. Our approach has the definite advantage of clearly distinguishing two tasks. One task is to obtain accurate numerical results; the other is to apply the theory, which may be revised and have its constants adjusted many times. One does not need to conduct a new simulation for each value of the constant. Direct simulations are also easier numerically, because the viscosity is uniform. On the other hand, in situations and geometries more complex than the present ones it would be more difficult to produce a global theory of the flow, as is needed in our approach, whereas the large-eddy simulation needs only a theory of small-scale turbulence, which is presumed to be equally valid in any geometry.

Direct simulations may be more suitable for fundamental research, but large-eddy simulations may be preferable for engineering applications.

2. Description of the flow and dimensional analysis

The fluid domain is the half space $[-\infty, \infty] \times [0, \infty] \times [-\infty, \infty]$ in the x-, y- and z-directions. At the wall, $y = 0$, the no slip condition applies the velocity vector: $\boldsymbol{U} \equiv (u, v, w) = 0$. In the free stream, $y \to \infty$, the velocity vector is prescribed as a function of time, but independent of x and z:

$$U_\infty = U_0 \cos(ft), \quad W_\infty = U_0 \sin(ft). \tag{1a, b}$$

The velocity vector describes a circle of radius U_0 centred at $(0, 0)$, and rotates at an angular rate f. The vorticity is zero outside the boundary layer. In the SB flow, (1*b*) was replaced by $W_\infty = 0$; there the interest was in strong two-dimensional pressure gradients and the reversal of the wall shear stress.

Inside the domain the incompressible Navier–Stokes equations apply. Disregarding the initial conditions, this problem has only three parameters, the velocity U_0, the frequency f, and the kinematic viscosity ν. The thickness of the laminar solution is $\delta_\ell \equiv (2\nu/f)^{\frac{1}{2}}$. The parameters combine into a single non-dimensional parameter, the Reynolds number

$$R_\ell \equiv \frac{U_0 \delta_\ell}{\nu} = U_0 \left(\frac{2}{f\nu}\right)^{\frac{1}{2}}. \tag{2}$$

We are seeking solutions that are statistically homogeneous in x and z and have been evolving long enough to lose memory of their initial condition. If the flow is laminar, the large-time solution is periodic:

$$U = U_0[\cos\phi - \mathrm{e}^{-y/\delta_\ell} \cos(\phi - y/\delta_\ell)], \quad V = 0, \quad W = U_0[\sin\phi - \mathrm{e}^{-y/\delta_\ell} \sin(\phi - y/\delta_\ell)],$$

where $\phi \equiv ft$ is the phase angle. If it is turbulent we expect the statistics, obtained by averaging over x and z, to be again time-periodic. We can expect this behaviour, as opposed to one in which the solution 'runs away' with quantities like the displacement thickness growing without bounds, because the symmetry of the free-stream motion (over a period $2\pi/f$) precludes the accumulation of momentum in any particular direction.

We also note that the equations and boundary conditions are invariant under the combined effects of a shift in time by an arbitrary amount T and a rotation by an angle fT. If we express the turbulence statistics with respect to a reference frame that has the same invariance property (e.g. one aligned with the instantaneous free-stream velocity vector), we further expect that they will be independent of phase angle once the flow is fully developed. This expectation was supported by the numerical results; after sufficient integration time and for a broad range of initial conditions we obtained either the laminar solution, or a turbulent one with statistics that satisfied the invariance property. In this respect, the present problem is simpler than the SB flow; that flow retained a genuine dependence on ϕ.

A rather extensive notation is needed because we shall alternate between various velocity scales, lengthscales, and reference frames for the normalization of the results. This will appear less gratuitous when the theory is presented in §§3 and 4. Here we introduce enough notation to express concisely what we mean by a fully developed turbulent solution. The brackets $\langle\ \rangle$ or a capital letter denote an average

in x and z, e.g. $U \equiv \langle u \rangle$, and a prime denotes a fluctuation, e.g. $u' \equiv u - U$. We use the notation $U^\times$ for the normalized velocity U/U_0, and so on. We use $\tilde{}$ to denote the components of vectors or tensors referred to free-stream axes. For instance $\tilde{u} \equiv u\cos\phi + w\sin\phi$. Thus we shall encounter notations like $\langle \widetilde{uw} \rangle^\times$. Other axes will be used later; they all have the same invariance property (under a shift in time by T). The $\tilde{}$ and similar qualifiers will be omitted whenever a quantity does not depend on the axes, e.g. v or $u^2 + w^2$. The distance from the wall can be normalized by δ_ℓ or by the outer lengthscale $L \equiv U_0/f$.

A fully developed solution is one in which the statistics, properly normalized and expressed in appropriate axes, are independent of time (or phase angle). Thus a quantity like $\langle \widetilde{uw} \rangle^\times$ is a function only of y/δ_ℓ at a given Reynolds number. The theory below rests primarily on assertions about the Reynolds-number dependence.

3. Basic theory

Up to this point we have presented rigorous dimensional arguments and some very plausible, qualitative arguments about the large-time behaviour of the solutions. In this section and the next we introduce some much stronger, quantitative assumptions, presumed to be valid only at high Reynolds numbers. With this in mind, the comparison of the theory and the numerical results can be very instructive, and the theory if validated will be useful in predicting quantitative aspects of flows at engineering and geophysical Reynolds numbers. The derivation owes much to Coles' 1956 paper. The basic theory is equivalent to Kazanski & Monin's (1961) or Csanady's (1967) work on the Ekman layer. The arguments are well known, and will be presented without detailed justification. In §4, at the expense of one further assumption we derive an extra term that is far from negligible at the low Reynolds numbers considered here.

We consider only the mean-velocity profiles and the Reynolds stresses and examine the consequences of the usual assumption that the flow contains an inner and an outer region, each with its own scaling, and that the inner and outer laws agree to leading order in an overlap region. This procedure is strongly supported by experimental and numerical results at least in the case of two-dimensional flows without pressure gradient (Coles 1956; Spalart 1988). Furthermore, the inner law has been found over the years to be essentially universal.

3.1. *Notation*

For the analysis of the turbulent flows, new velocity scales, lengthscales and axes are needed. First a velocity scale u^* is introduced, and velocities normalized by u^* are denoted by the usual $+$ superscript: $u^+ \equiv u/u^*$, and so on. The ratio U_0/u^* will appear often and is denoted by Z. Thus $U^+ = ZU^\times$, and so on. Near the wall the lengthscale is the usual ν/u^*, and yu^*/ν is denoted by y^+. Away from the wall we assume that $1/f$ is the appropriate timescale for the large eddies (which generate the Reynolds shear stress), and therefore define the lengthscale $\delta \equiv u^*/f$. For symmetry we shall denote y/δ by y^-. The quantity $R_t \equiv \delta u^*/\nu = R_\ell^2/(2Z^2)$ is the relevant turbulent Reynolds number.

A reference frame is needed besides the one aligned with the free-stream vector; let it point in the direction $\phi + \phi^*$. We use the notation $\hat{}$ as opposed to $\tilde{}$ for free-stream axes; $\hat{u} \equiv u\cos(\phi + \phi^*) + w\sin(\phi + \phi^*)$, and so on. The ratio Z and the angle ϕ^* are functions of the Reynolds number, to be specified later.

The quantities involved in the theory are U, W, and the total stresses

$\tau_x \equiv \nu \mathrm{d}U/\mathrm{d}y - \langle u'v' \rangle$ and $\tau_z \equiv \nu \mathrm{d}W/\mathrm{d}y - \langle v'w' \rangle$. It is convenient to use complex notation in the (x, z)-plane; an underline will identify the complex quantities:

$$\underline{\tilde{U}} \equiv \tilde{U} + \mathrm{i}\tilde{W}, \quad \underline{\tilde{\tau}} \equiv \tilde{\tau}_x + \mathrm{i}\tilde{\tau}_z, \tag{3}$$

and similarly for the $\hat{}$ variables. These functions satisfy $\underline{\tilde{U}} = \mathrm{e}^{\mathrm{i}\phi^*}\underline{\hat{U}}, \underline{\tilde{\tau}} = \mathrm{e}^{\mathrm{i}\phi^*}\underline{\hat{\tau}}$, $\underline{U}(0) = 0$, $\underline{\tilde{U}}^{\times}(\infty) = 1$. The mean (Reynolds-averaged) momentum equation is

$$\mathrm{i}(\underline{\tilde{U}}^{\times} - 1) = \frac{\mathrm{d}\underline{\tilde{\tau}}^{\times}}{\mathrm{d}(y/L)}, \tag{4}$$

which can be written in the other coordinates, e.g. $\mathrm{i}(\underline{\tilde{U}}^{+} - Z) = \mathrm{d}\underline{\tilde{\tau}}^{+}/\mathrm{d}y^{-}$.

3.2. *Definition of u^* and ϕ^**

In the basic theory the wall-shear stress vector $\nu[\mathrm{d}U/\mathrm{d}y(0), \mathrm{d}W/\mathrm{d}y(0)]$ gives both u^* and ϕ^*. u^* is identified to the friction velocity u_τ, given by $u_\tau^4 \equiv \nu^2[(\mathrm{d}U/\mathrm{d}y)^2 + (\mathrm{d}W/\mathrm{d}y)^2]$ (as a result Z is related to the friction coefficient by $Z = [2/C_f]^{\frac{1}{2}}$). ϕ^* is identified with the angle α that the wall-stress vector makes with the free stream, i.e. $\tan(\alpha) \equiv (\mathrm{d}\tilde{W}/\mathrm{d}y)/(\mathrm{d}\tilde{U}/\mathrm{d}y)$. To be concise, the choices $u^* \equiv u_\tau$ and $\phi^* \equiv \alpha$ ensure that $\hat{\underline{\tau}}^{+}(0) = 1$.

3.3. *Outer region*

Here we choose u^* for the velocity scale, δ for the lengthscale and the ϕ^* reference frame and assert that this normalization makes the velocity defect (the deviation from the free-stream value) and the shear stress independent of Reynolds number, i.e. $\underline{\hat{U}}^{+} - \mathrm{e}^{-\mathrm{i}\phi^*} Z$ and $\hat{\underline{\tau}}^{+}$ are functions of y^{-} only. We call these unknown, non-dimensional, complex functions f_1 and f_2:

$$\underline{\hat{U}}^{+} - \mathrm{e}^{-\mathrm{i}\phi^*} Z = f_1(y^{-}), \quad \hat{\underline{\tau}}^{+} = f_2(y^{-}). \tag{5a, b}$$

Because of the definition of δ this is compatible with the momentum equation which becomes $\mathrm{i}f_1 = f_2'$ where the prime denotes a derivative.

3.4. *Inner region*

Here we again choose u^* for the velocity scale, and the ϕ^* reference frame, but the lengthscale is ν/u^* and we consider the velocity with respect to the wall instead of with respect to the free stream. With a rough wall the roughness height would replace ν/u^*. Thus we assert that $\underline{\hat{U}}^{+}$ and $\hat{\underline{\tau}}^{+}$ are functions of y^{+} only:

$$\underline{\hat{U}}^{+} = f_3(y^{+}), \quad \hat{\underline{\tau}}^{+} = f_4(y^{+}). \tag{6a, b}$$

3.5. *Overlap region*

We assume the existence of an overlap region in which (5a) and (6a) both apply, and obtain

$$f_1(y^{-}) + \mathrm{e}^{-\mathrm{i}\phi^*} Z = f_3(y^{+}). \tag{7}$$

Recall that ϕ^* and Z are functions of R_ℓ, as is the ratio $y^{+}/y^{-} = R_t$, so that (7) depends on both y and R_ℓ. We first hold R_ℓ fixed and differentiate (7) with respect to $\log(y)$, to obtain

$$\frac{\mathrm{d}f_1}{\mathrm{d}(\log y^{-})} = \frac{\mathrm{d}f_3}{\mathrm{d}(\log y^{+})}. \tag{8}$$

We now vary the Reynolds number and therefore the ratio y^{+}/y^{-}; (8) can hold only if both sides equal a constant. We do not consider skewing in the wall region at this level of approximation; the constant is real and is identified with the inverse of the

Kármán constant, $df_1/d(\log y^-) = df_3/d(\log y^+) = 1/\kappa$. We arrive at the usual logarithmic law; $f_3 = \log(y^+)/\kappa + C$, $f_1 = \log(y^-)/\kappa + A$, where C is real but A is complex. Note that there are several other ways to arrive at the log law. Equation (7) becomes

$$A + e^{-i\phi^*} Z = \frac{1}{\kappa} \log R_t + C. \tag{9}$$

Its real and imaginary parts are

$$Z \cos\phi^* = \frac{1}{\kappa} \log R_t + C - A_r, \tag{10}$$

$$\sin\phi^* = \frac{A_i}{Z}. \tag{11}$$

Equivalent equations were obtained by Csanady (1967) for the Ekman layer over a rough wall. Equation (10) primarily involves the friction coefficient and the Reynolds number, and is similar to the two-dimensional equation. The most interesting prediction of this theory is (11), which has no equivalent in two dimensions. It is valid over smooth and rough walls, and implies that at high Reynolds numbers ϕ^* tends to zero, although slowly (like $1/\log R_\ell$). Thus the Ekman-like spiral becomes increasingly shallow as R_ℓ increases. To validate the theory, we can test (10) and (11). Directly testing the local assumptions (5), (6) will be helpful, if we restrict them to the appropriate regions.

4. Higher-order theory

We found that the basic theory (specifically, (10) and (11)) is not in good agreement with the numerical results, but that the agreement improves slightly at higher Reynolds numbers. This prompted us to regard that theory as providing only the leading term of an expansion in terms of the Reynolds number, and to derive a higher-order term which had the potential of improving the agreement at the low Reynolds numbers we treated. The arguments are just as simple as in the basic theory; we are not proposing a more elaborate concept of what generates and controls the shear stress. However, we do need to be specific about which of the properties of the constant-stress layer (e.g. the log layer, or the linear growth of the mixing length, or another property) remain valid with a non-constant stress, and which are violated. This is a matter of controversy and we made our choice primarily based on our numerical results in the present flow and in the sink flow (Spalart 1986*b*). Note that in both of these flows the stress variation is caused by a favourable pressure gradient; if it were caused by suction, or compressibility, a different behaviour may be observed. One may even wonder what the effect of a strong adverse gradient would be (Perry & Schofield 1973); the results in the SB flow tend to support our assumption, but are not fully conclusive.

4.1. *Definition of u^* and ϕ^**

To improve an asymptotic theory, especially one that is rather empirical, the first step is to identify its most severe inconsistency. The starting point is the fact that (6*a*) and (6*b*) are not compatible with the momentum equation, which can be written

$$i(\hat{\underline{U}}^+ - e^{-i\phi^*} Z) = R_t \frac{d\hat{\underline{\tau}}^+}{dy^+}. \tag{12}$$

In the basic theory we simply observed that as R_t becomes large (12) implies $d\hat{\underline{\tau}}^+/dy^+ \ll 1$, meaning that $\hat{\underline{\tau}}^+ = 1$ to leading order. Equation (6*b*) was never used. We propose to refine the theory enough for the momentum equation to be exactly satisfied, even at finite R_ℓ. Locally this is not a small change, but the wall region is thin, so that globally it results in a higher-order correction.

We also observed that if (5*a*) and (5*b*) apply the momentum equation is satisfied if $if_1 = f_2'$. This implies that in the viscous sublayer, where (5*a*) does not apply, (5*b*) cannot apply either. The direction of the shear stress rapidly varies in the wall region. To accommodate this in the theory we need to redefine ϕ^*; the new definition is equal to α only to leading order. Note that the deep reason for introducing ϕ^* as a variable is that the differential equations (not the boundary conditions) governing the flow are invariant by rotation. In the two-dimensional time-dependent flow an arbitrary phase shift was introduced for similar reasons. The only reason for assuming $\phi^* = \alpha$ earlier was the possibility that (5*b*) would apply all the way to the wall ($y^- = 0$). We now recognize that this is true only to leading order. On the other hand, u^* is still taken equal to u_τ (presumably, at even higher orders u^* would differ slightly from u_τ), and therefore instead of $\hat{\underline{\tau}}^+(0) = 1$ we have

$$\hat{\underline{\tau}}^+(0) = e^{i(\alpha-\phi^*)}. \tag{13}$$

Numerical results obtained in the sink flow (Spalart 1986*b*) and here strongly indicate that the law of the wall (6*a*) is very general and in particular is insensitive to pressure gradients. This is with u^* defined as the square root of the shear stress at the wall. Incidentally, this contradicts any theory that uses the local shear stress for a velocity scale, as well as those that assume that the mixing length still varies linearly when there is a pressure gradient (Berg 1975). This will be illustrated in figure 9. In summary our approach is to preserve (6*a*) near the wall, (5*a*) and (5*b*) away from the wall, and to demand that the momentum equation (4) be exactly satisfied everywhere. We surrender any equation of the type of (6*b*), and do not require that ϕ^* equal α.

4.2. *Implementation*

In order to apply the momentum equation all the way from the wall to the free stream we first obtain a composite expansion for the velocity profile. We define the function f_5 as the deviation from the log law in the viscous sublayer:

$$f_5(y^+) \equiv f_3(y^+) - \left[\frac{\log y^+}{\kappa} + C\right]. \tag{14}$$

The function f_5 is real and for y^+ larger than about 50, $f_5(y^+)$ is identically zero. The composite expansion is then written:

$$\hat{\underline{U}}^+ - e^{-i\phi^*} Z = f_1(y^-) + f_5(y^+). \tag{15}$$

Compare with (5*a*). Implicitly, we are extending f_1 down to $y^- = 0$ by a log layer. This procedure is standard in the field of matched asymptotic expansions (Van Dyke 1975), although we cannot pretend to be as systematic as if we had a well-defined, closed set of equations to solve. It is very similar to Coles' (1956) procedure, but we preferred to include the log component in f_1 rather than in f_5. This brings out a finite universal constant (C_5) (independent of three-dimensionality or pressure gradient), as shown below.

We combine the momentum equation $d\underline{\tau}^+/dy^- = i(\hat{\underline{U}}^+ - e^{-i\phi^*} Z)$ with (15) and

integrate with respect to y^- to express the global momentum balance. We obtain

$$\hat{\underline{\tau}}^+(0) = -\mathrm{i}\left[C_1 + \frac{C_5}{R_\tau}\right], \tag{16}$$

where

$$C_1 \equiv \int_0^\infty f_1(y^-)\,\mathrm{d}y^-, \quad C_5 \equiv \int_0^{50} f_5(y^+)\,\mathrm{d}y^+. \tag{17a, b}$$

The upper bound in the C_5 integral is not critical. However the uncertainty in the values of κ and C and the fact that C_5 is obtained as the difference of two numbers, each about 10 times as large as C_5 itself, introduce an uncertainty of the order of 10% for C_5. We computed $C_5 \approx -52$ from numerical two-dimensional flat-plate data, assuming $\kappa = 0.41$ and $C = 5$ (see the appendix in Spalart 1988, where it was called $-D_3$). Coles (1968) used a fit to experimental data and obtained a somewhat larger value: $C_5 = -64$, again with $\kappa = 0.41$ and $C = 5$. This difference is not large enough to invalidate the conclusions to be drawn in §5.

In the basic theory, $C_1 = \mathrm{i}$ and C_5 is neglected. In the higher-order theory we are interested in the term of order $1/R_\tau$. To that order, using (13) and (16) we obtain again $C_1 = \mathrm{i}$, and

$$\phi^* = \alpha + \frac{C_5}{R_\tau}. \tag{18}$$

This defines ϕ^*, superseding the assumption $\phi^* = \alpha$ of the basic theory, and completes the higher-order theory. As expected the difference between α and ϕ^* is of higher order than their values (which are of order $1/Z$). The form of (10) and (11) is unaffected. Note that *a priori* the law of the wall (6*a*) should be applied in a reference frame directed at an angle α, not ϕ^*. However, the difference between the two is too small to affect the theory at this order.

5. Numerical results

5.1. *Parameters and numerical details*

Results will be presented at $R_\ell = 500$, 620 and 767. The lowest value is close to the minimum at which turbulence can be sustained (at $R_\ell = 400$, the flow relaminarized); the other two were chosen to provide a geometric progression of the turbulent Reynolds number R_τ, with a ratio of about $\sqrt{2}$. R_τ took the values 466, 653, and 914. Periodic conditions were used in the homogeneous directions, and the size of the numerical periods scaled with δ: $\Lambda_x = \Lambda_z \approx 2\delta$. The thickness of the turbulent region is about δ. The effect of Λ_x and Λ_z was tested by rerunning the $R_\ell = 500$ case with $\Lambda_x = \Lambda_z \approx 4\delta$ and the same grid spacing, time step, and so on. The values of Z and ϕ^* were altered by less than 0.5%. The differences in the velocity, stress and budgets profiles were also insignificant. This test indicates that periods equal to 2δ are sufficiently large, at least for our purpose. In contrast to two-dimensional flows, the constant change of direction of the flow presumably prevents the formation of very long structures in the streamwise direction.

The grid spacing was $\Delta x^+ = \Delta z^+ \approx 7$, and in the y-direction there were at least ten grid points within 10 wall units of the wall (same resolution as in Spalart 1988). The grids had $128 \times 50 \times 128$, $192 \times 64 \times 192$, and $256 \times 80 \times 256$ collocation points at the three Reynolds numbers. The spectral numerical method was described by Spalart (1986*a*). Observe that the resolution was chosen using the same lengthscales (δ and ν/u^*) that entered the theory. However, this does not mean that the validation of the theory is circular, because the results are not (and must not be) significantly

dependent on the resolution. This is confirmed by the test of Λ here, and the test of grid spacing by Spalart (1988).

The initial conditions were the sum of the laminar profile and random disturbances of finite amplitude, typically $\pm 20\%$ of U_0. Since only the turbulent state is of interest there is no point in starting from small disturbances (in addition, the turbulence appears to be subcritical). When available, the final state of a lower-Reynolds-number simulation was used as the initial condition. While the flow was being established, a coarser grid was used; halving the number of points in each direction reduces the computer cost per unit time by a factor of about 20, with the present method. Simulations on such coarse grids produce acceptable large eddies (having longer timescales, these take more time to establish) but are not accurate enough near the wall, since they may overpredict the friction coefficient by as much as 20% at a given Reynolds number (Spalart 1988, figure 2). With a spectral method it is a simple matter to interpolate from one grid to another; the interpolation is often done in steps, for instance from 128 points to 192, and then to 256 for the 'true' simulation.

Another helpful measure, before the statistics are taken, is an over-relaxation procedure applied to the mean profile. This profile often approaches its steady state in a very sluggish manner (especially when the pressure gradient is held constant, as opposed to the mass flux). The implementation is slightly more involved than for flows with steady boundary conditions. Let us write the momentum equation, formally, $\mathrm{d}u/\mathrm{d}t = rhs$. It may be split into mean and fluctuations (the Fourier series used in x and z do this naturally) to produce: $\mathrm{d}U/\mathrm{d}t = \langle rhs \rangle \equiv RHS$, $\mathrm{d}u'/\mathrm{d}t = rhs'$. The latter equation is not amenable to over-relaxation, because of the stability limitations of the Runge–Kutta time-integration scheme. On the other hand the mean component is a good candidate since it is in the process of approaching a steady state, and is much less susceptible to numerical instability. For convenience we switch to complex notation again: $\mathrm{d}\underline{U}/\mathrm{d}t = \underline{RHS}$. Now since $\underline{U} = \mathrm{e}^{\mathrm{i}\phi}\tilde{U}$ we have $\mathrm{d}\underline{U}/\mathrm{d}t = \mathrm{i}f\underline{U} + \mathrm{e}^{\mathrm{i}\phi}\mathrm{d}\tilde{U}/\mathrm{d}t$. Then the equation driving $\tilde{U}$ is $\mathrm{d}\tilde{U}/\mathrm{d}t = \mathrm{e}^{-\mathrm{i}\phi}[\underline{RHS} - \mathrm{i}f\underline{U}]$; when equilibrium is reached $\underline{RHS}$ (which contains the pressure gradient and the shear stress) and $\mathrm{i}f\underline{U}$ are in balance, which amounts to (4). During the transient we artificially accelerate the evolution of $\tilde{U}$ by writing $\mathrm{d}\tilde{U}/\mathrm{d}t = \Omega\mathrm{e}^{-\mathrm{i}\phi}[\underline{RHS} - \mathrm{i}f\underline{U}]$, where Ω is a number larger than 1. In terms of $\underline{U}$ itself (which is the variable used in the code) this equation is $\mathrm{d}\underline{U}/\mathrm{d}t = \Omega[\underline{RHS} - \mathrm{i}f\underline{U}] + \mathrm{i}f\underline{U}$. Essentially, we devised an equation that differs from the Navier–Stokes equation, but has the same steady state, and reaches it faster. Values of Ω up to 10 have been used without stability problems, depending on the grid, Reynolds number, and so on. In practice this device makes the approach to the steady state several times as fast as would happen otherwise. It can be easily used for other flows including two-dimensional boundary layers, channels, and Ekman layers (with steady boundary conditions, it reduces to $\mathrm{d}U/\mathrm{d}t = \Omega\ RHS$).

The stability of the time integration is enhanced by solving the equations with respect to a reference frame that is moving at a velocity intermediate between that of the wall and that of the free stream. At best, on small-disturbance problems, this allows one to double the time step without losing the numerical stability. In a turbulent flow, the gain is typically a 50% increase in the allowable time step, which is appreciable. Furthermore, the time step is continually adjusted to yield a prescribed peak Courant number; as a result it can be set close to the stability limit, without any risk of numerical instability. Overall, the measures taken to contain the cost of the simulations (using restart files, coarse grids during transients, over-

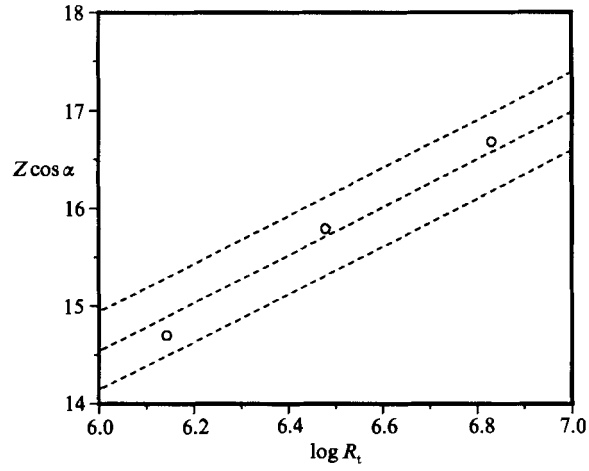

FIGURE 1. Comparison of basic theory and numerical results. ---, (10) with $\phi^* = \alpha$, $\kappa = 0.41$, and various values of A_r; ○, simulations.

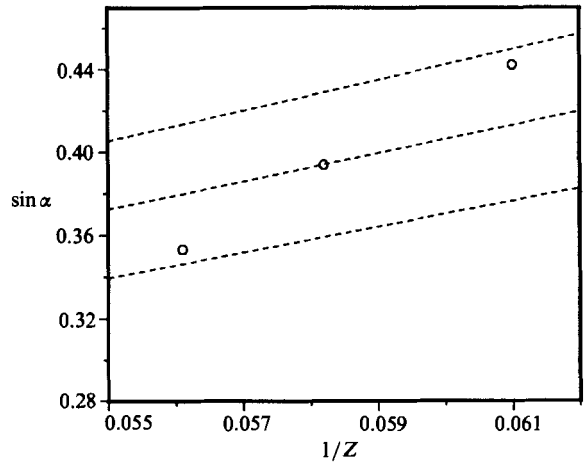

FIGURE 2. Comparison of basic theory and numerical results. ---, (11) with $\phi^* = \alpha$ and various values of A_i; ○, simulations.

relaxation, and so on) probably reduced it by a factor close to 10, compared with a straightforward strategy. Even then, the cost was in excess of 10^{14} operations.

Fully developed solutions were obtained in the sense that Z, α, and quantities like the peak turbulent kinetic energy reached stable values and then only varied slightly. The time-sample length for the statistics was at least $1.8/f$, which combined with the spatial average over an area $(2\delta)^2$ was sufficient to produce very smooth profiles and balanced momentum and energy budgets over the whole depth of the turbulent layer. The global momentum balance (the integral of (4)) was satisfied to within 1%. Far from the wall (y^- larger than about 0.8) the timescales of the turbulence are longer, making the effective sample smaller, so that the end of the spiral on the hodograph is not perfectly smooth. Note that the prominent quantities (u^*, ϕ^*) result from the near-wall behaviour.

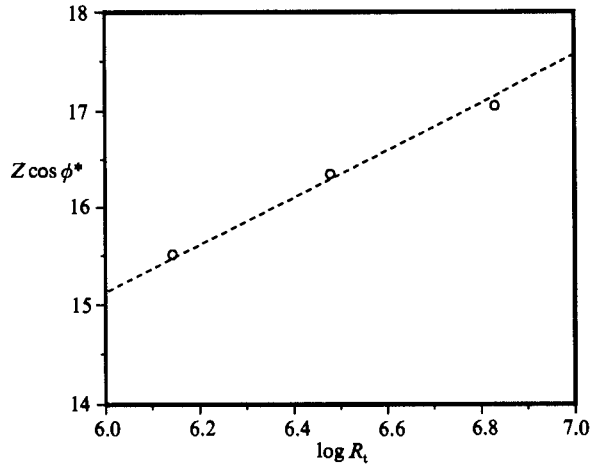

FIGURE 3. Comparison of higher-order theory and numerical results. ---, (10) with ϕ^* given by (18), $\kappa = 0.41$, $C_5 = -52$, and $A_r - C = -0.45$; ○, simulations.

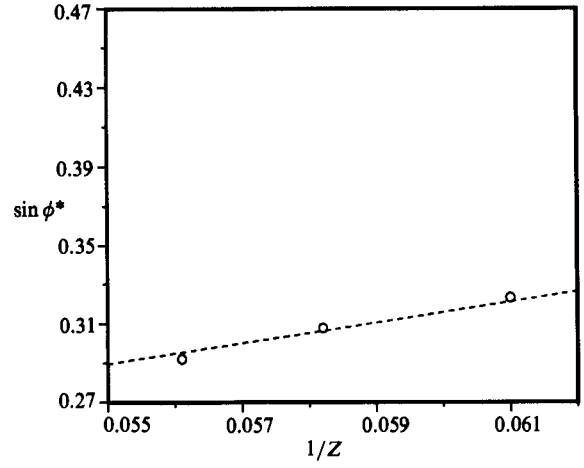

FIGURE 4. Comparison of higher-order theory and numerical results. ---, (11) with ϕ^* given by (18), $\kappa = 0.41$, $C_5 = -52$, and $A_i = 5.5$; ○, simulations.

5.2. *Global results*

At Reynolds numbers $R_\ell = 500$, 620, and 767 the values of u^*/U_0 (i.e. $1/Z$) were 0.0610, 0.0583, and 0.0561 respectively. They are typical of low-Reynolds-number boundary layers. The values of α were 0.458, 0.405, and 0.365 radians. These are much lower than the laminar value ($\frac{1}{4}\pi \approx 0.89$) and decrease as R_ℓ increases, as predicted by the theory. Figures 1 and 2 are tests of the basic theory; the agreement with (10) is fair, but with (11) it is unsatisfactory in that the slopes of the theoretical and numerical curves differ by a factor close to 3. In figures 3 and 4, the higher-order theory is used and the agreement is excellent. The values $\kappa = 0.41$ and $C_5 = -52$ were used throughout. Based on (18), the values of ϕ^* are 0.347, 0.325, and 0.309 at the three Reynolds numbers. The results indicate that the values of the adjustable constants are $A_r \approx 4.6 \pm 0.3$ and $A_i \approx 5.5 \pm 0.3$. The uncertainty reflects the slight disagreement remaining in figures 3 and 4, and the uncertainty on the values of κ, C, and C_5. The agreement is much better than in the SB flow; this is most probably

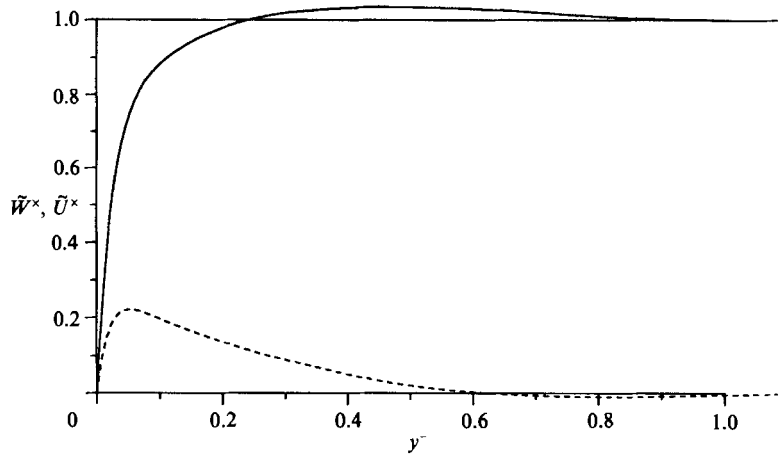

FIGURE 5. Mean velocity profiles. $R_\ell = 500$. —— $\tilde{U}^\times$, --- $\tilde{W}^\times$.

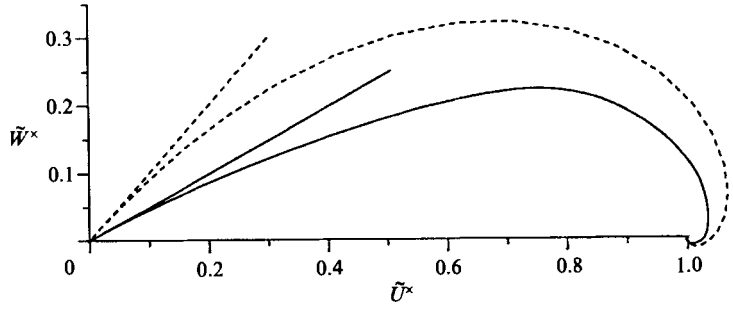

FIGURE 6. Hodograph, $\tilde{W}^\times$ versus $\tilde{U}^\times$. ---, laminar flow; ——, turbulent flow, $R_\ell = 500$.

because the present flow is constantly turbulent, whereas the two-dimensional flow experienced partial relaminarization near the wall twice per cycle.

We may compare the values of the adjustable constants with the ones prevailing in the Ekman layer. We are not at all implying that they should be equal; although the scaling arguments are the same in the two flows, the physics of the large eddies are not, especially if the latitude of the Ekman layer is not $\frac{1}{2}\pi$ (Coleman *et al.* 1989). Csanady (1967) reports experimental values between 7 and 12 for A_i, a much larger scatter than in our results. Townsend (1976) quotes $A_1 = 10.7$. Note that they both relied on the basic theory, which overestimates A_i (in our results at $R_\ell = 500$, $Z \sin\alpha$ equals 7.2 but $Z \sin\phi^* = 5.6$). For A_r, the comparison is not possible because Csanady considered rough surfaces. In this flow, as in the SB flow, the ϕ^* equation (11) is independent of the type of surface, but the other equation (10) is not.

5.3. *Local results*

We now present local quantities to describe the flow in more detail and to test the local assumptions, (5) and (6). The higher-order equation (18) is used to define ϕ^* for the remainder of the paper. It gives consistently better collapse of the results at different Reynolds numbers, although the difference is often slight. Figure 5 presents the mean velocity profiles $\tilde{U}^\times$ and $\tilde{W}^\times$, displaying the overshoot and the skewing. The peak value of the cross-flow $\tilde{W}^\times$ is about 20% of the free-stream velocity. In figure 6 the hodograph $\tilde{W}^\times$ versus $\tilde{U}^\times$ is found to be much shallower in turbulent than in

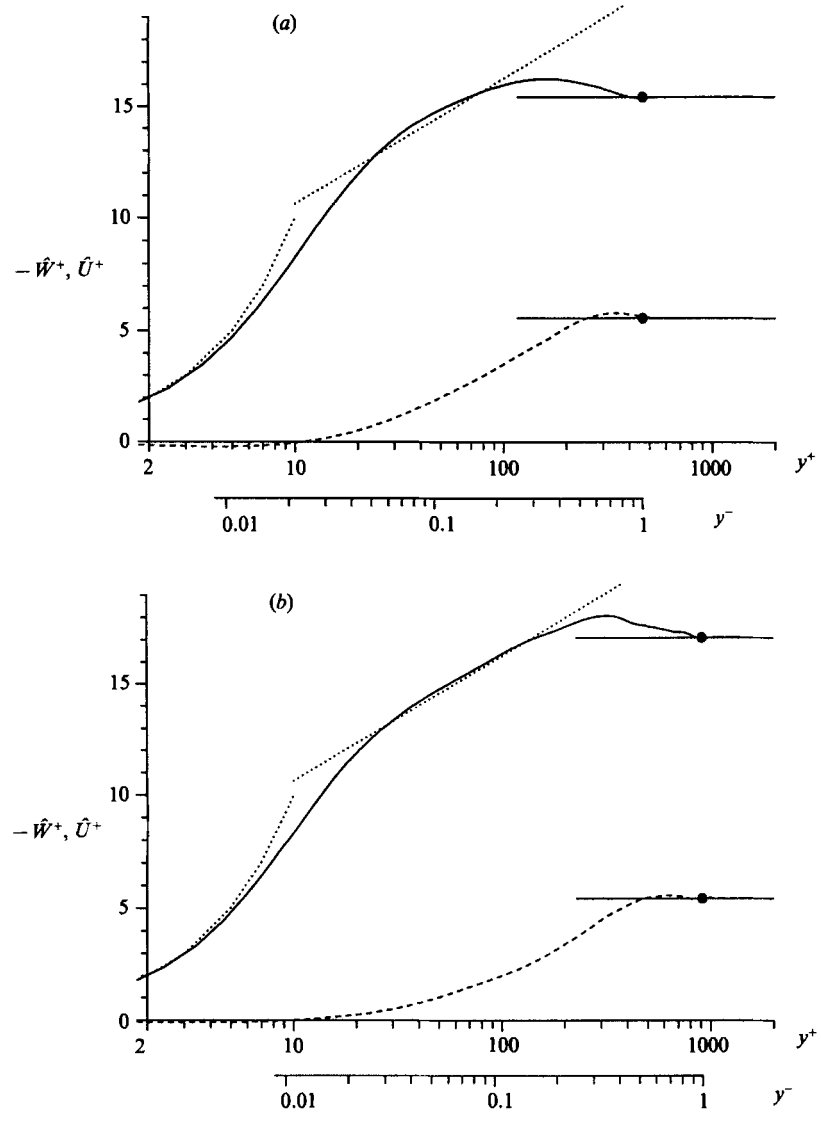

FIGURE 7. Mean-velocity profiles. (*a*) $R_\ell = 500$; (*b*) $R_\ell = 767$. ——, $\hat{U}^+$; – – –, $-\hat{W}^+$; ●, location of δ; straight line $\log(y^+)/0.41 + 5$. ϕ^* given by (18).

laminar flow. This is consistent with the behaviour of turbulent Ekman layers. The tangents at the origin indicate the size of α.

Figure 7 tests assumption (6*a*). $\hat{U}^+$ and $-\hat{W}^+$ are shown in a semilogarithmic plot versus y^+. Equation (6*a*) is strongly supported by the results: at fixed y^+, $\hat{U}^+$ becomes Reynolds-number independent over a larger range and $|\hat{W}^+|$ decreases with Reynolds number. Note that $\hat{U}^+$ varies much less than $\hat{W}^+$ as a function of R_ℓ. The plot also reveals a long logarithmic layer at $R_\ell = 767$, very close to the usual $f_3 = \log(y^+)/0.41 + 5$.

Figure 7 can also be used to test assumption (5*a*), by examining the curves with reference to the solid circles, placed at $y = \delta$, and the free-stream velocity (a y^- scale is also provided). One is then considering $\hat{U}^+(y^-) - \hat{U}^+_\infty$ and $\hat{W}^+(y^-) - \hat{W}^+_\infty$, the quantities that enter (5*a*). The agreement between figures 7 (*a*) and 7 (*b*) is good down

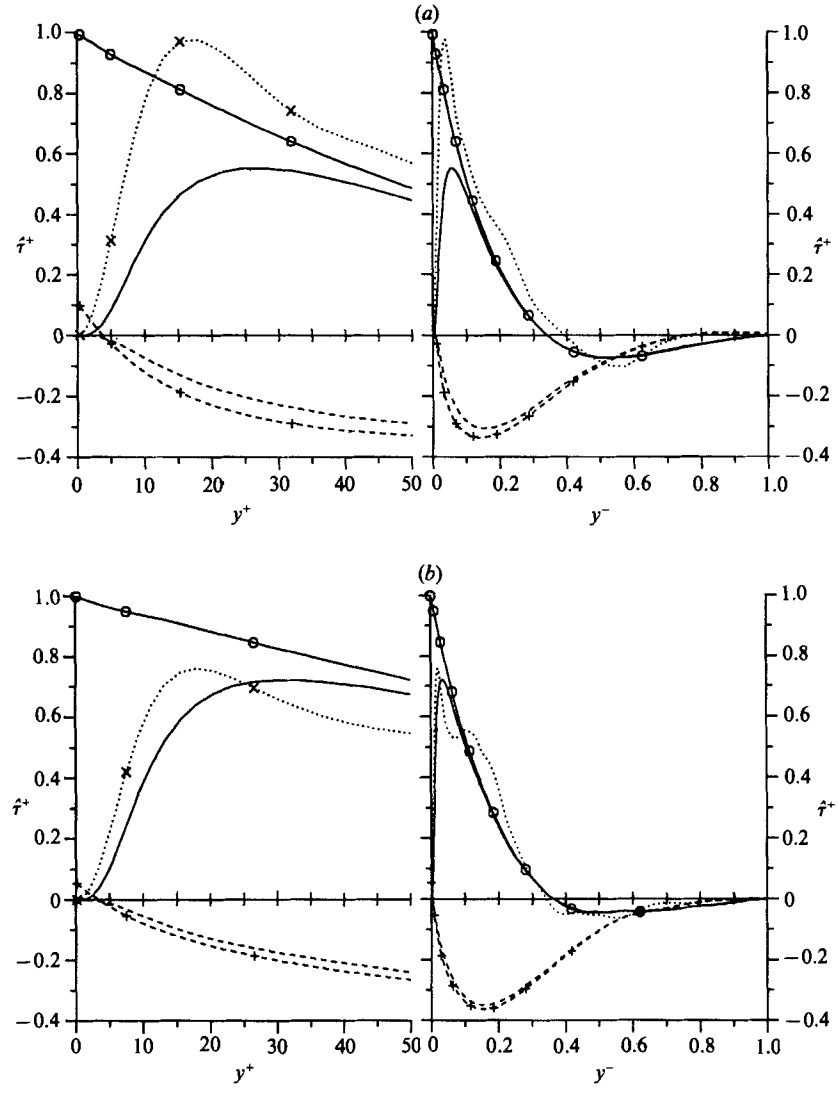

FIGURE 8. Reynolds and total shear stresses. (*a*) $R_\ell = 500$; (*b*) $R_\ell = 767$. –○–, $\hat{\tau}_x^+$; ——, $-\langle\widehat{u'v'}\rangle^+$; –+–, $\hat{\tau}_z^+$; – – –, $-\langle\widehat{w'v'}\rangle^+$; · · × · ·, $-\langle\widehat{u'w'}\rangle^+$. ϕ^* given by (18).

to $y^- \approx 0.1$. The upper part of the $R_\ell = 767$ curve is a little rough, but the figure clearly supports the assumptions made for the velocity profile (5*a*), (6*a*).

In figure 8 the Reynolds and total shear stresses are shown at $R_\ell = 500$ and 767. We are testing assumptions (5*b*) and (6*b*); ϕ^* axes and the u^* velocity scale are used. For this and most of the remaining figures composite plots were made with the wall region up to $y^+ = 50$ and the outer region up to $y^- = 1$. In the outer layer (right side) the comparison is very good. For $\hat{\tau}_z^+$, the figure illustrates the rapid turning near the wall that was mentioned earlier. The figure shows conclusively that the Reynolds-number independence of the shear stresses would not be obtained with the δ_ℓ lengthscale, because the ratio δ/δ_ℓ increases by a factor 1.4 from $R_\ell = 500$ to 767 (on the other hand, the ratio δ/L (equal to $1/Z$) changes by only 9%, so that the results would be about as good if plotted versus y/L instead of y^-). Similarly, the velocity

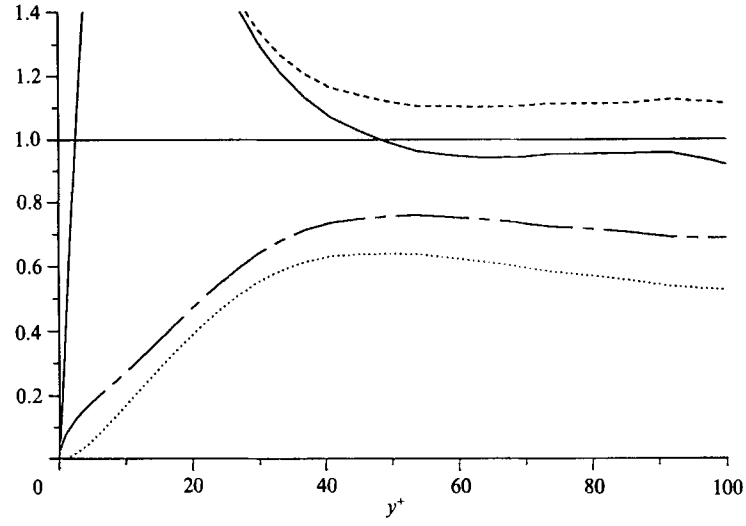

FIGURE 9. Test of various assumptions in the wall region. $R_\ell = 767$. ——, $\kappa \mathrm{d}\hat{U}^+/\mathrm{d}(\log y)$; – – –, $\kappa|\mathrm{d}\underline{U}^+/\mathrm{d}(\log y)|$; · · ·, $|\underline{\tau}^+_{\mathrm{R}}|/[\kappa|\mathrm{d}\underline{U}^+/\mathrm{d}(\log y)|]$; – – – –, $|\underline{\tau}^+_{\mathrm{R}}|^{\frac{1}{2}}/[\kappa|\mathrm{d}\underline{U}^+/\mathrm{d}(\log y)|]$.

scale U_0^2 is ruled out because $(u^*/U_0)^2$ varies by 19%. Finally, the free-stream axes would give about as good results as the ϕ^* axes away from the wall, but not near the wall since $\tilde{\underline{\tau}}^+$ is not close to 1.

Near the wall, figure 8 confirms that (6*b*) is far from being satisifed, but that at a fixed y^+ value $\underline{\tau}^+$ approaches 1 as R_ℓ increases, i.e. the near-wall layer becomes more two-dimensional and is closer to being a constant-stress layer. The stress gradient in wall units is proportional to Z^3/R_ℓ^2 and therefore tends to zero rapidly. Note that the magnitude of the total stress decreases away from the wall; in that sense the pressure gradient is favourable. Note also that with the higher-order theory $\hat{\tau}_z^+$ is not exactly 0 at the wall, because ϕ^* is not exactly equal to α. Near the wall the third shear stress, $-\langle\widehat{u'w'}\rangle^+$, takes rather large values and exhibits a significant dependence on R_ℓ. Its peak value decreases from 0.97 at $R_\ell = 500$ to 0.65 at $R_\ell = 767$. Away from the wall $-\langle\widehat{u'w'}\rangle^+$ shows no significant trend versus Reynolds number. Note that this Reynolds stress has no effect on the mean flow, since the flow is homogeneous in the x- and z-directions. This would not be the case, for example, on a swept wing. However this stress would only have a weak effect in the mean momentum equation, and thus attention has been focused on $-\langle u'v'\rangle^+$ and $-\langle v'w\rangle^+$ (Bradshaw 1987).

Figure 9 supports the decision made to preserve (6*a*), rather than (6*b*) or assumptions about the behaviour of the eddy viscosity or the mixing length, in a more direct manner than figures 1–4 did. The quantities $\kappa \mathrm{d}\hat{U}^+/\mathrm{d}(\log y)$, $\kappa|\mathrm{d}\underline{U}^+/\mathrm{d}(\log y)|$, $|\underline{\tau}^+_{\mathrm{R}}|/[\kappa|\mathrm{d}\underline{U}^+/\mathrm{d}(\log y)|]$, and $|\underline{\tau}^+_{\mathrm{R}}|^{\frac{1}{2}}/[\kappa|\mathrm{d}\underline{U}^+/\mathrm{d}(\log y)|]$ are shown in the wall region of the flow at $R_\ell = 767$. Here τ_{R} is the Reynolds stress. The first two quantities stem from two- and three-dimensional versions of the log law, the third is the ratio of the eddy viscosity to $\kappa y u^*$, and the fourth is the ratio of the mixing length to κy. In a classical constant-stress layer, for y^+ larger than about 50 all these quantities equal 1. We find here, as we did in the sink flow, that under the effect of a favourable pressure gradient the quantities derived from the log law deviate from 1 much less than those derived from the eddy viscosity or mixing length. If we had plotted the square of the mixing length, which may be equitable since it is what enters the turbulence model, the difference would be even larger. Note that the two- and three-

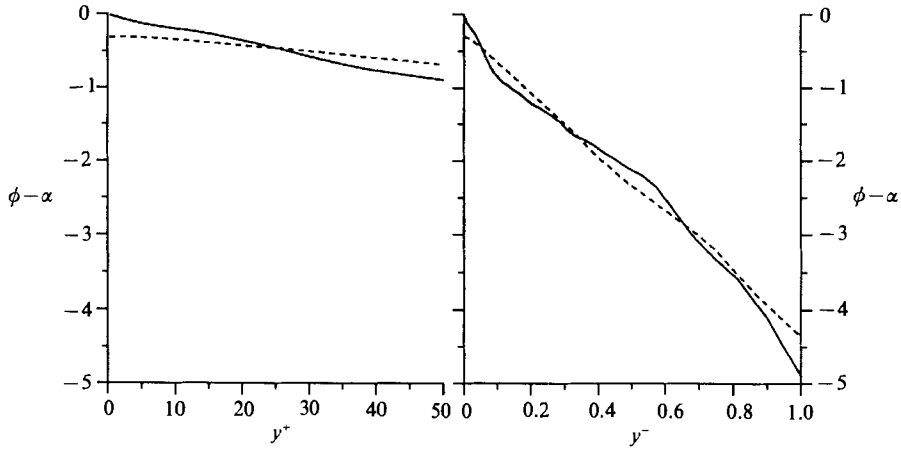

FIGURE 10. Direction of the mean-shear and Reynolds-stress vectors. $R_\ell = 500$. ——, $(\mathrm{d}\hat{U}/\mathrm{d}y, \mathrm{d}\hat{W}/\mathrm{d}y)$; – – –, $(-\widehat{\langle u'v'\rangle}, -\widehat{\langle v'w'\rangle})$.

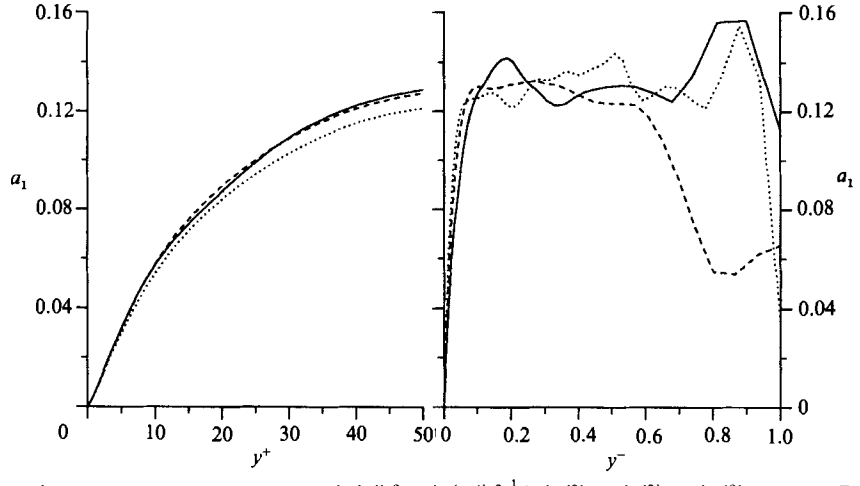

FIGURE 11. Structure parameter. $a_1 \equiv [\langle u'v'\rangle^2 + \langle u'w'\rangle^2]^{\frac{1}{2}}/(\langle u'^2\rangle + \langle v'^2\rangle + \langle w'^2\rangle)$. ——, $R_\ell = 500$; – – –, $R_\ell = 620$; · · ·, $R_\ell = 767$.

dimensional log laws bracket the ideal value of 1, with the two-dimensional version performing appreciably better. The higher-order definition of ϕ^* was used; with the basic definition, the two-dimensional law is not quite as good.

The shear stresses are considered again in figures 10 and 11. Figure 10 compares the direction of the mean-shear vector $(\mathrm{d}U/\mathrm{d}y, \mathrm{d}W/\mathrm{d}y)$ and the Reynolds-stress vector $(-\langle u'v'\rangle, -\langle v'w'\rangle)$. The curves are rather rough away from the wall, because they represent the ratio of small quantities, but one can still draw the following conclusions. The directions are close throughout the layer, usually within 10°, suggesting that in the present flow the turbulence is only weakly three-dimensional. This test was conducted by Deardorff (1970) in the Ekman layer, with the same result. The direction of the larger principal axis of the tensor $(\langle u'^2\rangle, \langle u'w'\rangle, \langle u'w'\rangle, \langle w'^2\rangle)$ was also examined and found to be very close to the ones plotted in figure 10. Figure 11 shows the structure parameter, the ratio of the modulus of the shear stress to the trace of the Reynolds-stress tensor (Bradshaw, 1967). Its average value away

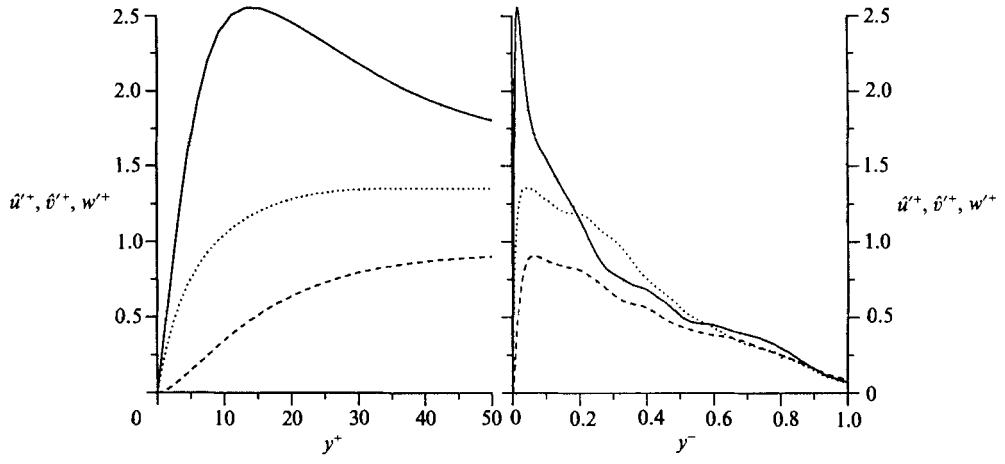

FIGURE 12. R.m.s. of the velocity components. ——, $[\langle\hat{u}'^2\rangle^+]^{\frac{1}{2}}$; – – –, $[\langle\hat{v}'^2\rangle^+]^{\frac{1}{2}}$; · · ·, $[\langle\hat{w}'^2\rangle^+]^{\frac{1}{2}}$. $R_\ell = 767$. ϕ^* given by (18).

from the wall is about 0.13, appreciably lower than the usual two-dimensional values, which are 0.15 to 0.16; this is consistent with experimental observations in three-dimensional flows (Bradshaw 1987). The curves are too rough for one to distinguish a Reynolds-number trend; according to the theory, a_1 will be slightly lower at high Reynolds numbers.

The behaviour of the normal Reynolds stresses $\langle\hat{u}'^2\rangle^+$, $\langle\hat{v}'^2\rangle^+$, and $\langle\hat{w}'^2\rangle^+$ is predictable, see figure 12. Recall that they slightly increase with Reynolds number (Spalart 1988). They are close to the usual two-dimensional values near the wall, and farther up $\langle\hat{w}'^2\rangle^+$ becomes larger than $\langle\hat{u}'^2\rangle^+$, because of the skewing. The undulations seen for y^- larger than 0.2 would be removed by a longer time sample, but the trend for $\langle\hat{w}'^2\rangle^+$ to exceed $\langle\hat{u}'^2\rangle^+$ is genuine and is observed at all Reynolds numbers.

5.4. *Reynolds-stress budgets*

The budgets of the six Reynolds stresses and the trace of the tensor are shown in figure 13. All the terms add up to zero very well near the wall, and rather well away from the wall, considering the expanded scale. The viscous term is not split into diffusion and dissipation. The diffusion can be computed from the Reynolds stresses themselves, if desired. The same applies to the convection term and the production. The time-dependent term arises because the reference frame is not fixed. This term is absent for the trace (figure 13*a*) and $\langle\hat{v}'^2\rangle^+$ (figure 13*c*) and is found to be small for the other terms (in addition, it decreases with increasing Reynolds number). This shows that the timescale $1/f$ is much longer than the scales on which the turbulence is produced and dissipated. Deardorff (1970) observed the same trend and concluded that the rotation had very little effect on the turbulence. Such an inference ignores hidden effects such as a possible alteration of the triple-correlation terms, and must be made with caution. Curvature effects, for instance, are known to be much larger than predicted from order-of-magnitude arguments.

In general the budgets follow the usual patterns. The Reynolds-number dependence is weak except for $-\langle\widehat{u'w'}\rangle^+$ near the wall. Recall that the budgets were normalized by u^* and ν/u^* near the wall, and u^* and δ (or f) away from it, to be consistent with (5) and (6); ϕ^* axes were used. Notice the reversal of the pressure transfer between $\langle\hat{u}'^2\rangle^+$ and $\langle\hat{w}'^2\rangle^+$ away from the wall, and the sign change of the

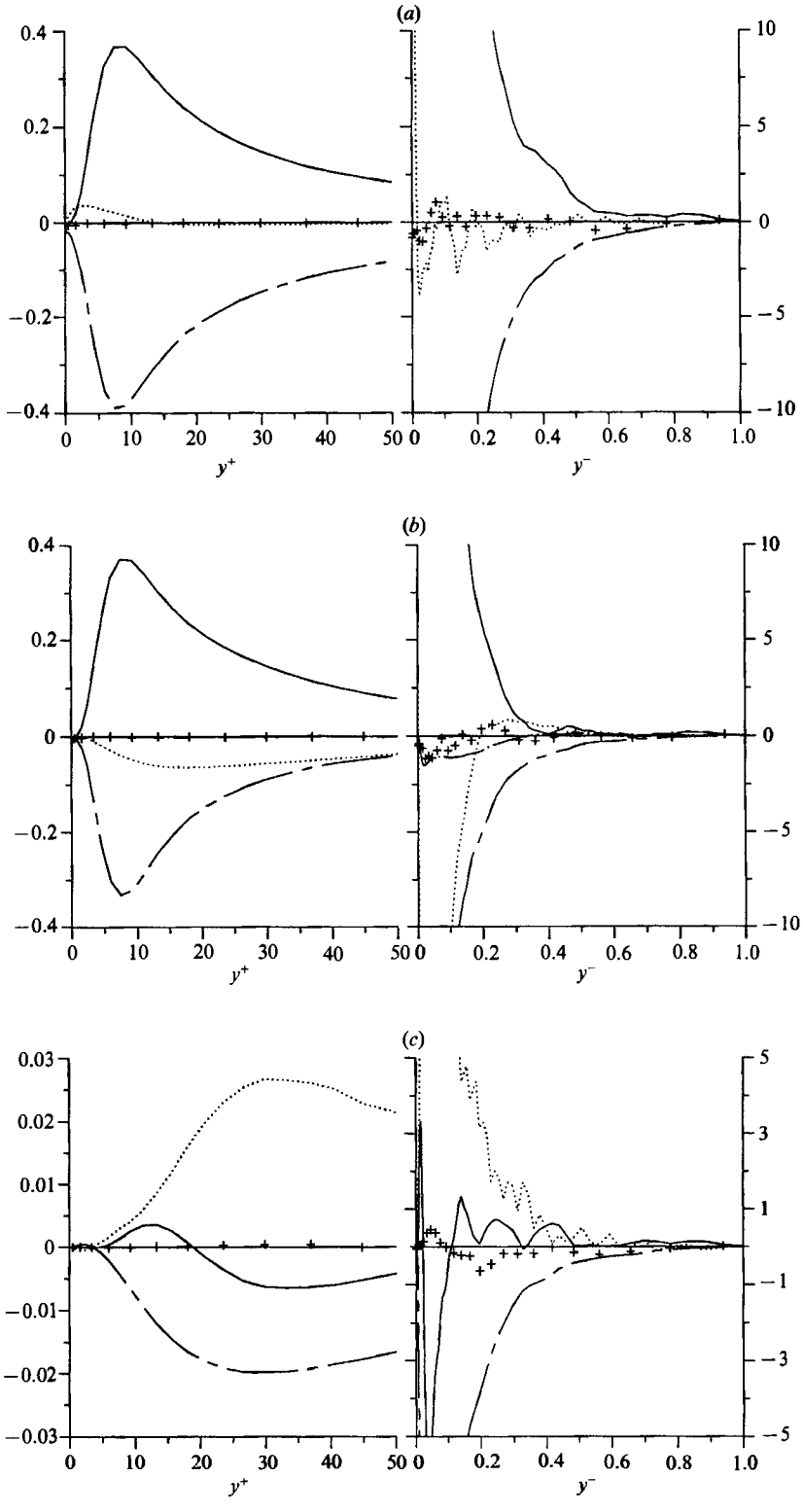

FIGURE 13(*a–c*). For caption see p. 338.

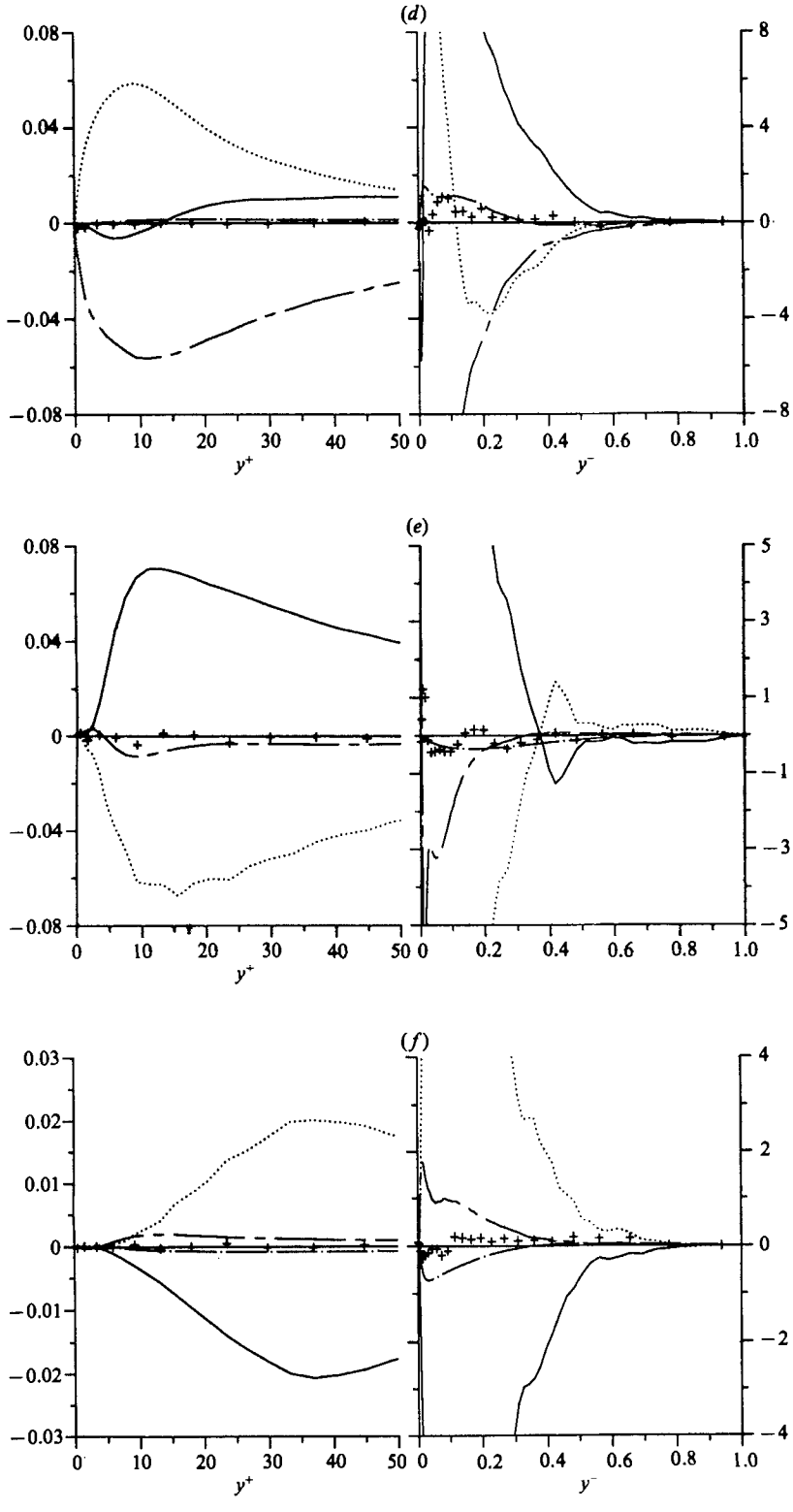

FIGURE 13(*d–f*). For caption see p. 338.

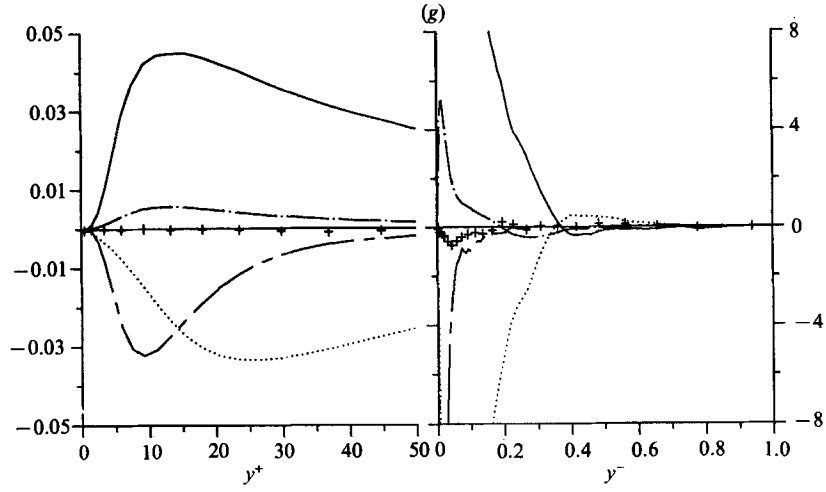

FIGURE 13. Budgets of the Reynolds stresses. $R_\ell = 767$. ——, convection term; – – –, viscous term; · · ·, pressure term; · — ·, time-dependent term; +, total. Left plot normalized by u^{*4}/ν; right plot by u^{*3}/δ. (*a*) $\langle \hat{u}'^2 \rangle^+ + \langle \hat{v}'^2 \rangle^+ + \langle \hat{w}'^2 \rangle^+$; (*b*) $\langle \hat{u}'^2 \rangle^+$; (*c*) $\langle \hat{v}'^2 \rangle^+$; (*d*) $\langle \hat{w}'^2 \rangle^+$; (*e*) $-\langle \widehat{u'v'} \rangle^+$; (*f*) $-\langle \widehat{v'w'} \rangle^+$; (*g*) $-\langle \widehat{u'w'} \rangle^+$. ϕ^* given by (18).

contributions to $-\langle \widehat{u'v'} \rangle^+$ near $y^- = 0.3$. The $-\langle \widehat{u'w'} \rangle^+$ budget is dominated by the convection term (turbulent diffusion), on the gain side, and the viscous and pressure terms, on the loss side. The time-dependent term is weak, which suggests that the non-zero $-\langle \widehat{u'w'} \rangle^+$ stress is primarily due to diffusion from other elevations where the tensor has a different orientation, and not from the local effect of the tensor lagging the reorientation at a rate f.

6. Discussion and conclusions

Direct numerical simulations of a simple turbulent boundary layer that is three-dimensional in the mean were conducted. The flow is homogeneous in the directions parallel to the wall, so that no multiple-scale approximation or inflow–outflow conditions were needed. The turbulence was found to be only weakly three-dimensional, as measured by the close alignment of the Reynolds stresses with the mean shear, or the comparison of the rotation rate with the timescales of the turbulence. This reflects the gradual application of three-dimensionality. Incidentally, this makes the flow difficult to classify as either shear-driven or pressure-driven (Bradshaw 1987). A sudden application could easily be implemented with the present method, but the analysis of the results will be much more involved and one may need a costly ensemble average (T.-H. Shih, personal communication). The present results should still be useful for the initial tests of turbulence models with three-dimensional capabilities. The structure parameter is appreciably lower than in two-dimensional flows.

The numerical results, both local and global, entirely support the set of Reynolds-number scaling laws that was presented. The theoretical arguments also apply to an important geophysical flow, the turbulent Ekman layer (however, the two flows are likely to differ quantitatively, notably in the values of the adjustable constants A_r and A_i). The basic theory, equivalent to published theories of the Ekman layer, gave fair agreement with local quantities but failed to accurately predict some of the more

sensitive quantities, namely the magnitude and direction of the wall shear stress. The direction is the most sensitive quantity. A higher-order theory was derived, based on the same arguments but refined to satisfy the momentum equation across the entire domain. With this theory the agreement is excellent, and we can extrapolate to high Reynolds numbers with confidence.

The higher-order theory was developed to explain the numerical results; however, it could have been developed independently. The key steps (retaining (6*a*) even with pressure gradient and using (4) instead of (6*b*)) are supported by numerical evidence gathered in the sink flow, the oscillating flow, and the present flow. We do not know of any rigorous theoretical argument that could prove or disprove them, and cannot estimate with full confidence how general they are. It may even be that they are valid only for favourable pressure gradients. Note also that the higher-order term has no equivalent in two dimensions, and that the idea of requiring the momentum equation to be exactly satisfied may not be so helpful in spatially developing flows, because the momentum equation is then quite unwieldy (Berg 1975).

The importance of the higher-order term in real planetary boundary layers is probably slight. We base this estimate on the fact that the correction (18) is roughly equal to $y_{\log}/\delta$ where $y_{\log}$ is the location at which the velocity profile first agrees with the log law (this occurs for $y^+_{\log} \approx 50$, and $|C_5| \approx 50$). Over rough terrain, $y_{\log}$ may be a few tens of metres at most, so if δ is a few kilometres, (18) yields $\alpha - \phi^*$ of the order of 0.01. In that case, the higher-order term is not needed in planetary-boundary-layer models. It is, however, very important for the validation of the theory using low-Reynolds-number simulation results, and to obtain accurate values for A_r and A_i.

Finally, it is remarkable that, even at Reynolds numbers close to the minimum at which turbulence is sustained (and with values of u^*/U_0 in excess of 0.06) the comparison of theory and numerical results appears free of the parasitic 'low-Reynolds-number effects' that effect the two-dimensional flat-plate boundary layer (Coles 1962). One would have expected the simpler steady two-dimensional flow to agree better with the theory. Here we must add a note of caution; our own simulations of the flat-plate layer also revealed weaker low-Reynolds-number effects than found by Coles, as measured by the strength of the wake (although there were other issues involved such as the accurate measurement of u_τ, and the exact values of κ and C). That disagreement remains unexplained, even after some of the obvious possible causes (such as lack of numerical resolution) were explored (Spalart 1988). On the other hand the multiple-scale approximation, used in the flat-plate flow, was not needed here. In that respect the present simulations are more reliable.

The author thanks Dr J. Buell and Mr G. Coleman of NASA Ames Research Center for reviewing the manuscript. Professor P. Bradshaw of Stanford University made a number of excellent suggestions. Some of the calculations were performed on the NAS computers.

REFERENCES

BERG, B. VAN DEN 1975 A three-dimensional law of the wall for turbulent shear flows. *J. Fluid Mech.* **70**, 149–160.

BRADSHAW, P. 1967 The turbulence structure of equilibrium boundary layers. *J. Fluid Mech.* **29**, 625–645.

BRADSHAW, P. 1987 Turbulent secondary flows. *Ann. Rev. Fluid Mech.* **19**, 53–74.

COLEMAN, G. N., FERZIGER, J. H. & SPALART, P. R. 1989 A numerical study of the turbulent Ekman layer. *J. Fluid Mech.* submitted.

COLES, D. E. 1956 The law of the wake in the turbulent boundary layer. *J. Fluid Mech.* **1**, 191–226.

COLES, D. E. 1962 The turbulent boundary layer in a compressible fluid. Appendix A: A manual of experimental practice for low-speed flow. pp. 35–74. *Rand. Rep.* R403-PR, ARC 24473.

COLES, D. E. 1968 The young person's guide to the data. *Proc. AFOSR-IFP-Stanford Conf. on Computation of Turbulent Boundary Layers, Stanford, Calif., Aug. 18–25, 1968*, Vol. 2, p. 1–45.

CSANADY, G. T. 1967 On the resistance law of a turbulent Ekman layer. *J. Atmos. Sci.* **24**, 467–471.

DEARDORFF, J. W. 1970 A three-dimensional numerical investigation of the idealized planetary boundary layer. *Geophys. Fluid Dyn.* **1**, 377–410.

KAZANSKI, A. B. & MONIN, A. S. 1961 On the dynamical interaction between the atmosphere and the earth's surface. *Bull. Acad. Sci. USSR, Ser. Geophys.* **5**, 514–515.

MASON, P. J. & THOMSON, D. J. 1987 Large-eddy simulations of the neutral-static-stability planetary boundary layer. *Q. J. R. Met. Soc.* **113**, 413–443.

PERRY, A. E. & SCHOFIELD, W. H. 1973 Mean velocity and shear stress distributions in turbulent boundary layers. *Phys. Fluids.* **16**, 2068–2074.

SPALART, P. R. 1986*a* Numerical simulation of boundary layers. Part 1. Weak formulation and numerical method. *NASA TM* 88222.

SPALART, P. R. 1986*b* Numerical study of sink-flow boundary layers. *J. Fluid Mech.* **172**, 307–328.

SPALART, P. R. 1988 Direct simulation of a turbulent boundary layer up to $R_\theta = 1410$. *J. Fluid Mech.* **187**, 61–98.

SPALART, P. R. & BALDWIN, B. S. 1987 Direct simulation of a turbulent oscillating boundary layer. *Proc. 6th Symp. on Turbulent Shear Flows, Toulouse, France, Sept. 7–9, 1987.*

TOWNSEND, A. A. 1976 *The Structure of Turbulent Shear Flow*, 2nd edn. Cambridge University Press.

VAN DYKE, M. 1975 *Perturbation Methods in Fluid Mechanics* (annotated edn). Stanford: Parabolic.